ARTICLE

Microfluidization of Graphite and Formulation of Graphene-Based Conductive Inks

Panagiotis G. Karagiannidis,[†] Stephen A. Hodge,[†] Lucia Lombardi,[†] Flavia Tomarchio,[†] Nicolas Decorde,[†] Silvia Milana,[†] Ilya Goykhman,[†] Yang Su,[‡] Steven V. Mesite,[‡] Duncan N. Johnstone,[¶] Rowan K. Leary,[¶] Paul A. Midgley,[¶] Nicola M. Pugno,[§,⊥,||] Felice Torrisi,[†] and Andrea C. Ferrari[*,†]

[†]Cambridge Graphene Centre, University of Cambridge, Cambridge CB3 0FA, United Kingdom
[‡]Microfluidics International Corporation, Westwood, Massachusetts 02090, United States
[¶]Department of Materials Science and Metallurgy, University of Cambridge, Cambridge CB3 0FS, United Kingdom
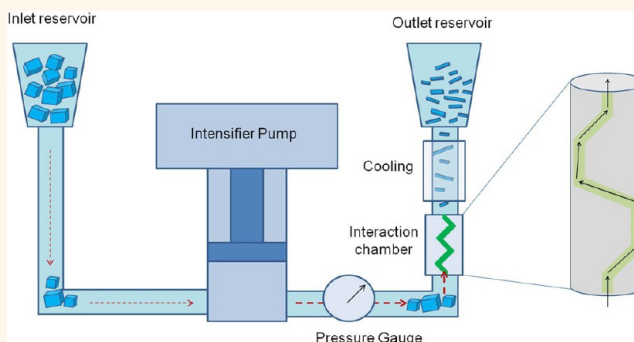[§]Department of Civil, Environmental and Mechanical Engineering, University of Trento, Trento 38123, Italy
[⊥]Fondazione Bruno Kessler, Center for Materials and Microsystems, Povo, Trento 38123, Italy
[||]School of Engineering and Materials Science, Queen Mary University, London E1 4NS, United Kingdom

ABSTRACT: We report the exfoliation of graphite in aqueous solutions under high shear rate $[\sim 10^8 \text{ s}^{-1}]$ turbulent flow conditions, with a 100% exfoliation yield. The material is stabilized without centrifugation at concentrations up to 100 g/L using carboxymethylcellulose sodium salt to formulate conductive printable inks. The sheet resistance of blade coated films is below $\sim 2\Omega/\square$. This is a simple and scalable production route for conductive inks for large-area printing in flexible electronics.

KEYWORDS: graphene, solution processing, flexible electronics, conducting inks

Printed electronics combines conducting, semiconducting, and insulating materials with printing techniques, such as inkjet,[1] flexography,[2] gravure,[3] and screen.[4] Metal inks based on Ag,[5] Cu,[6] or Au[7] are used due to their high conductivity $\sigma \sim 10^7$ S/m,[5,8,9] making them the dominant technology in high-frequency electronics (*e.g.* for radio frequency identification, RFID).[10,11] For flexible electronic devices, *e.g.*, organic photovoltaics (OPVs), a sheet resistance, R_s $[= 1/(\sigma h)$, where h is the film thickness$]$ $< 10\Omega/\square$ is required,[12] while for printed RFID antennas, one needs a few $\Omega/\square$.[13] To minimize R_s and cover the underneath rough layers, such as printed poly(3,4-ethylenedioxythiophene) polystyrene-sulfonate (PEDOT:PSS),[14] thick films (μm range) are deposited using screen printing.[1,14−16] This is a technique in which the ink is forced mechanically by a squeegee through the open areas of a stencil supported on a mesh of synthetic fabric.[17] The ink must have high viscosity, μ (>500 mPas),[18,19] because lower μ inks run through the mesh rather than dispensing out of it.[18] To achieve this μ, typical formulations contain a conductive filler, such as Ag particles,[20] and insulating additives,[17] at a total concentration higher than $C \sim 100$ g/L.[17] Of this, >60 g/L consist of the conductive filler needed to achieve high $\sigma \sim 10^7$ S/m.[20,21] In 2016, the average cost of Ag was $\sim$\$550/kg,[22] that of Au $\sim$\$40,000/kg,[22] while Cu was

cheaper at $\sim$\$4.7/kg.[23] Although metal oxidation issues under ambient conditions have been addressed as indicated in refs 6 and 24, metal electrodes can degrade the device performance, by chemically reacting with photoactive layers (Cu[25]) or by migrating into device layers (Cu,[26] Ag[27]). It was also reported that they might cause water toxicity,[28] cytotoxicity,[29] genotoxicity,[30] and deoxyribonucleic acid (DNA) damage.[31] The average cost of graphite in 2016 was $\sim$\$1/kg,[32] however, carbon-based inks are not typically used to print electrodes in OPVs or RFIDs, due to their low $\sigma \sim 2−4 \times 10^3$ S/m,[33−35] which corresponds to a $R_s \sim 20$ to $10\Omega/\square$ for a 25 μm film. Thus, there is a need for cheap, stable, and nontoxic conductive materials.

Graphene is a promising alternative conductive filler.[36] Graphite can be exfoliated *via* sonication using solvents[37−42] or water/surfactant solutions.[40,43] Dispersions of single layer graphene (SLG) flakes can be produced at concentrations $\sim$0.01g/L[37] with a yield by weight $Y_w \sim 1\%$,[37] where Y_w is defined as the ratio between the weight of dispersed material
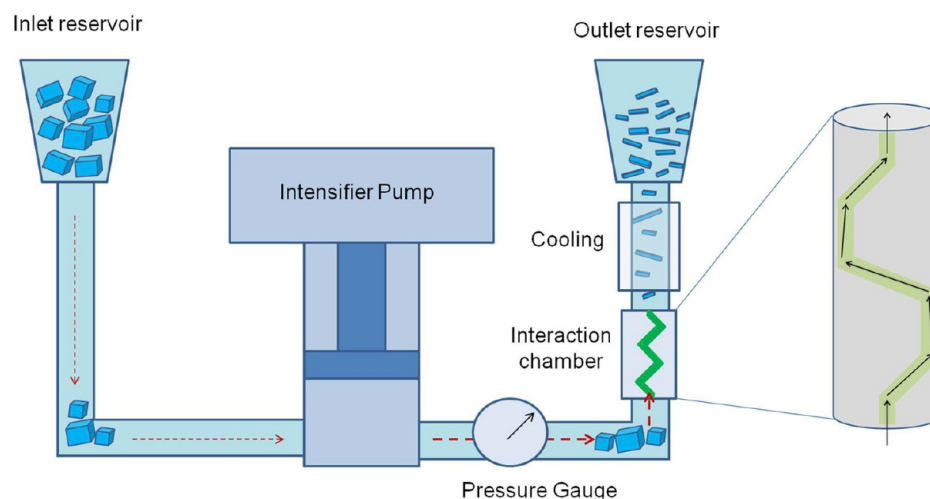
Figure 1. Schematic of the microfluidization process. Graphite flakes in SDC/water are added in the inlet reservoir. An intensifier pump applies high pressure (up to ~207 MPa) and forces the suspension to pass through the microchannel of the interaction chamber where intense $\dot{\gamma} \sim 10^8 s^{-1}$ is generated. The processed material is cooled and collected from the outlet reservoir. The process can be repeated several times.

and that of the starting graphite flakes.[44] Dispersions of few layer graphene (FLG) flakes (<4 nm) can be achieved with $C \sim$ 0.1 g/L[45] in N-methyl-2-pyrrolidone (NMP) and ~0.2 g/L in water.[40] The low $Y_w \sim$ 1−2%[40,45] for FLG prepared by bath sonication is due to the fact that a significant amount of graphite remains unexfoliated, as the ultrasonic intensity (i.e., the energy transmitted per unit time and unit area[46]) is not uniformly applied[46,47] and depends on the design and location of the ultrasonic transducers.[47] In tip sonication, the ultrasound intensity decays exponentially with distance from the tip[48] and is dissipated at distances as low as ~1 cm.[48] Therefore, only a small volume near the tip is processed.[49] Refs 50 and 51 reported ~2 nm thick flakes with a lateral size ~70 × 70 nm² and $C \sim$ 0.2 g/L with Y_w = 1% by tip sonication. In order to formulate screen printing inks,[51] the flakes C was increased from 0.2 g/L to 80 g/L via repetitive centrifugation (4 times) and redispersion (3 times) processes, resulting in an increased preparation time. Ref 52 used a rotor-stator mixer to exfoliate graphite, reaching C < 0.1 g/L of FLGs with Y_w < 2 × 10⁻³. Y_w is low because in mixers, a high shear rate, $\dot{\gamma}$, (i.e., the velocity gradient in a flowing material)[53] is localized in the rotor-stator gap[52,54] and is ~2 × 10⁴ to 1 × 10⁵ s⁻¹, dropping by a factor ~100 outside it.[54] Ref 55 reported the production of FLGs with number of layers N < 5 and Y_w > 70% through electrochemical expansion of graphite in lithium perchlorate/propylene carbonate. The process required 3 cycles of electrochemical charging followed by >10 h of sonication and several washing steps (with hydrochloric acid/dimethylformamide, ammonia, water, isopropanol, and tetrahydrofuran) to remove the salts. A method with less processing steps and high Y_w (ideally 100%) remains a challenge.

Microfluidization is a homogenization technique whereby high pressure (up to 207 MPa)[56] is applied to a fluid, forcing it to pass through a microchannel (diameter, d < 100 μm), as shown in Figure 1 and discussed in Methods. The key advantage over sonication and shear-mixing is that high $\dot{\gamma}$ > 10⁶ s⁻¹ is applied to the whole fluid volume,[57,58] not just locally. Microfluidization was used for the production of polymer nanosuspensions[56] in pharmaceutical applications to produce liposome nanoparticles to be used in eye drops[59] and aspirin nanoemulsions[60] as well as in food applications for oil-in-water

nanoemulsions.[61] Microfluidization was also used for the deagglomeration and dispersion of carbon nanotubes.[62]

Here, we report the production of FLG flakes with $Y_w \sim$ 100% by microfluidization. The dispersion is stabilized at a C up to ~100 g/L using carboxymethylcellulose sodium salt (CMC) (C = 10g/L). 4% of the resulting flakes are <4 nm, and 96% are in the 4 to 70 nm thickness range. The stabilized dispersion is used for blade coating and screen printing. R_s of blade coated films after thermal annealing (300 °C-40 min) reaches 2Ω/□ at 25 μm (σ = 2 × 10⁴S/m), suitable for electrodes in devices such as OPVs,[12,63] organic thin-film transistors (OTFTs),[64] or RFIDs.[13] The inks are then deposited on glass and paper substrates using blade coating and screen printing to demonstrate the viability for these applications (OPVs, OTFTs, RFIDs).

RESULTS AND DISCUSSION

We use Timrex KS25 graphite flakes as a starting material. They are selected because their size is suitable for flow in microchannels ~87 μm wide (90% are <27.2 μm).[65] Larger flakes would cause blockages. The flakes are used in conjunction with sodium deoxycholate (SDC) (Aldrich). SDC is first mixed in deionized (DI) water (σ = 5.5 × 10⁻⁶ S/m), and the flakes are then added and treated with a microfluidic processor with a Z-type geometry interaction chamber (M-110P, Microfluidics), Figure 1. Mixtures are processed at the maximum pressure for this system (~207 MPa), with varying process cycles (1−100). The temperature, T [°C], increases from 20 to 55 °C after the liquid passes through the interaction chamber. A cooling system then reduces it to ~20 °C. This is important, otherwise T will keep increasing and the solvent will boil. Graphite/SDC mixtures with increasing graphite C (1−100 g/L) and 9 g/L SDC in DI water are processed over multiple cycles (1, 5, 10, 20, 30, 50, 70, 100). One cycle is defined as a complete pass through the interaction chamber.

Scanning electron microscopy (SEM) (Figure 2a) is used to assess the lateral size of the starting flakes and of exfoliated flakes after 5, 20, and 100 cycles. Dispersions are diluted (1000 times, from 50 g/L to 0.05 g/L) to avoid aggregation after they
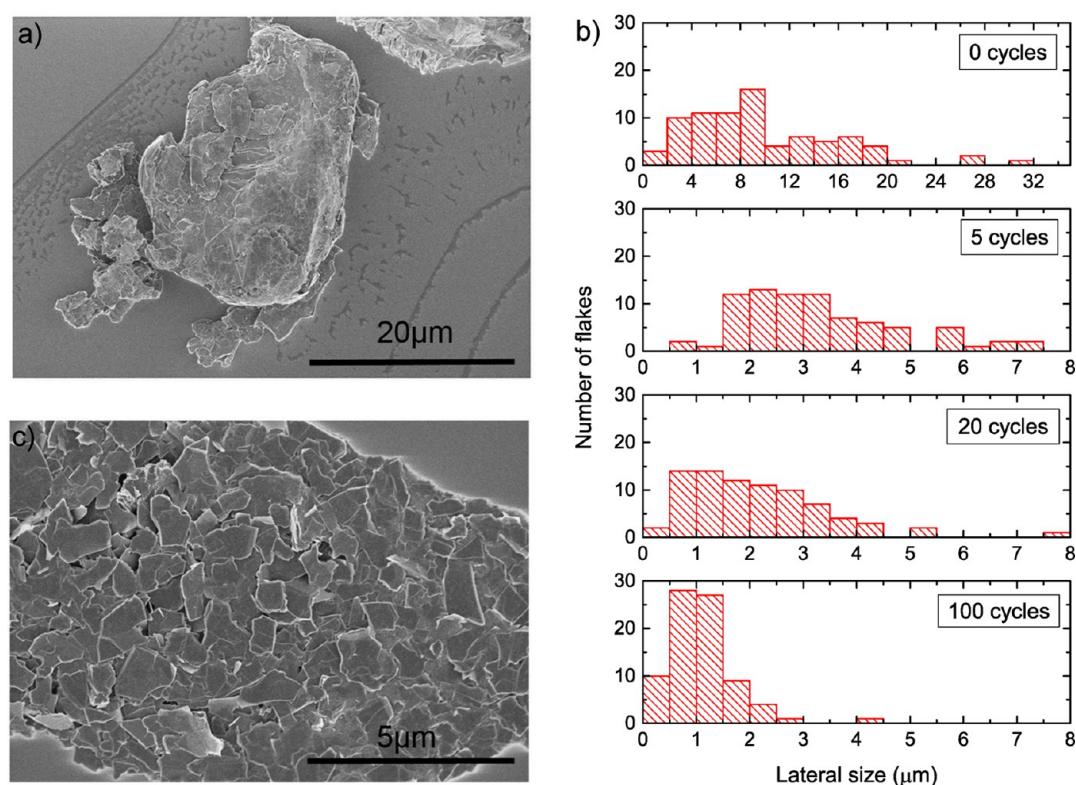
Figure 2. (a) SEM image of pristine graphite flakes. (b) Histograms of lateral flake size for the starting material and after 5, 20, and 100 cycles. (c) SEM image after 100 cycles.
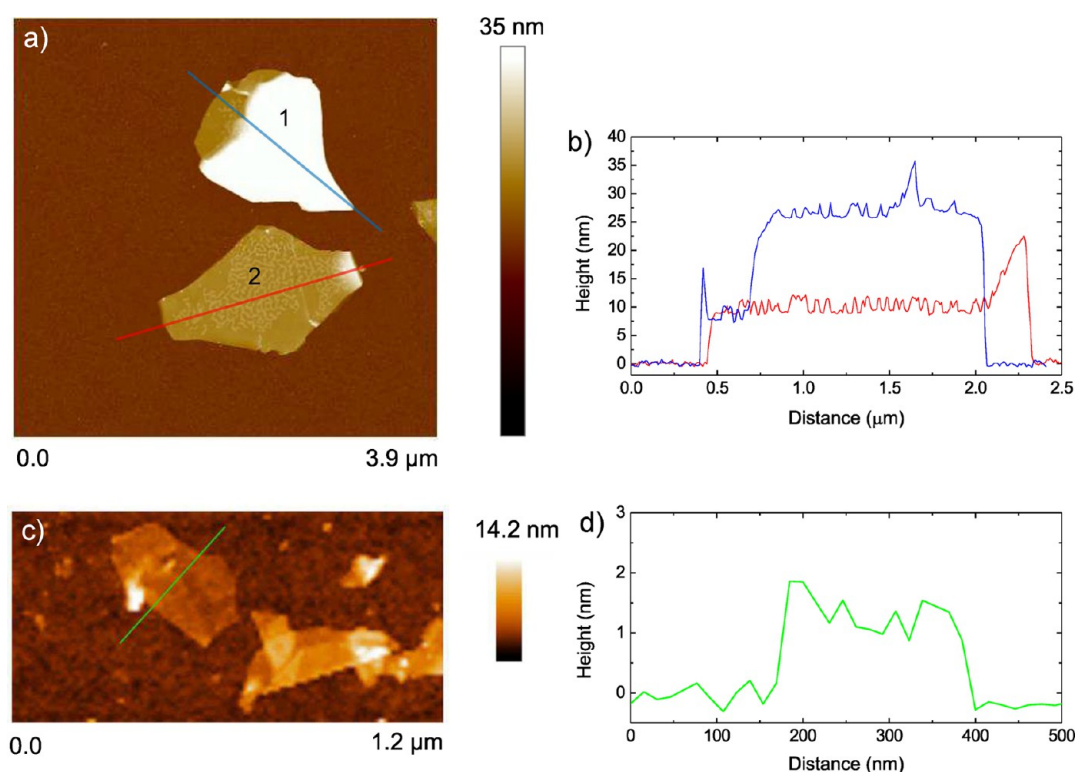

Figure 3. AFM images of typical flakes produced after 20 cycles: (a) flakes with $h = 25$ nm (1) and 8.5 nm (2). (b) Corresponding cross section profiles. (c) Flakes with $h = 1$ nm and (d) corresponding cross section.

are drop cast onto Si/SiO$_2$. The samples are further washed with five drops of a mixture of water and ethanol (50:50 in volume) to remove the surfactant. Three different magnifica-

tions are used. For each, images are taken at 10 positions across each sample. A statistical analysis of over 80 particles (Figure 2b) of the starting graphite reveals a lateral size (defined as the

longest dimension) up to ~32 μm. Following microfluidization, this reduces, accompanied by a narrowing of the flake distribution. After 100 cycles (Figure 2c), the mean flake size is ~1 μm.

Atomic force microscopy (AFM) is performed after 20 and 100 cycles to determine the h and aspect ratio (AR = lateral size/h) using a Dimension Icon (Bruker). After 20 cycles, Figures 3a,b show flakes with $d \sim 1.7$ μm and $h = 25$ nm and $d = 1.9$ μm with $h = 8.5$ nm, while Figures 3c,d show ~1 nm flakes, consistent with N up to 3. AFM statistics of h and AR are also performed. Three samples, ~60 μL, are collected from each dispersion (20 and 100 cycles) and drop cast onto 1 cm × 1 cm Si/SiO$_2$ substrates. These are further washed with five drops of a mixture of water and ethanol (50:50 in volume) to remove the surfactant. AFM scans are performed at 5 different locations on the substrate with each scan spanning an area of ~20 μm × 20 μm. For each processing condition, we measure 150 flakes. After 20 cycles, h shows a log-normal distribution[66] peaked at ~10 nm (Figure 4a), with a mean value of ~19 nm. After 100 cycles (Figure 4a), the distribution is shifted towards a lower h, with a maximum at ~7.4 nm, a mean $h \sim 12$ nm (4% of the flakes are <4 nm and 96% are between 4 and 70 nm). Figure 4b shows that AR increases with processing cycles from ~41 for 20 cycles to ~59 for 100.

The crystalline structure of individual flakes is investigated after 100 cycles (no significant difference is observed between samples of different processing cycles) by performing scanning electron diffraction (SED)[67] using a Philips CM300 field emission gun transmission electron microscope operated at 50 kV fitted with a NanoMegas Digistar system.[68] This enables the simultaneous scan and acquisition of diffraction patterns with an external optical charge-coupled device (CCD) camera imaging the phosphor viewing screen of the microscope. Using SED, small angle convergent beam electron diffraction patterns are acquired at every position as the electron beam is scanned over 10 flakes with a step size of 10.6 nm. Local crystallographic variations are visualized by plotting the diffracted intensity in a selected subset of pixels in each diffraction pattern as a function of probe position to form so-called "virtual dark-field" images.[67,69] Figures 5a,c,e,g show the virtual dark-field images and Figures 5b,d,f,h, the corresponding diffraction patterns with integration windows marked. These show regions contributing to the selected Bragg reflection and therefore indicate local variations in the crystal structure and orientation. Consistent with selected area electron diffraction (SAED), three broad classes of flakes are observed, comprising: (a,b) single crystals, (c,d) polycrystals of numerous (>5) small crystals, and (e—h) polycrystals of few (<5) larger crystals. This shows that there is heterogeneity between individual flakes and that after 100 cycles a significant fraction (~70%) are polycrystalline.

It is important to assess any chemical changes, such as oxidation or other covalent functionalization, that might occur during processing, since unwanted basal plane functionalization may lead to a deterioration in electronic performance.[70] Flakes produced after 100 cycles are washed by filtration to remove SDC prior to thermogravimetric analysis (TGA) and X-ray photoelectron spectroscopy (XPS). For this washing procedure, 10 mL isopropanol is added to a 5 mL dispersion to precipitate the flakes. The resulting mixture is passed through a 70 mm diameter filter and rinsed with 500 mL of DI water followed by 500 mL of ethanol. The powder is dried under vacuum and scraped from the filter paper. Inert atmosphere (nitrogen) TGA
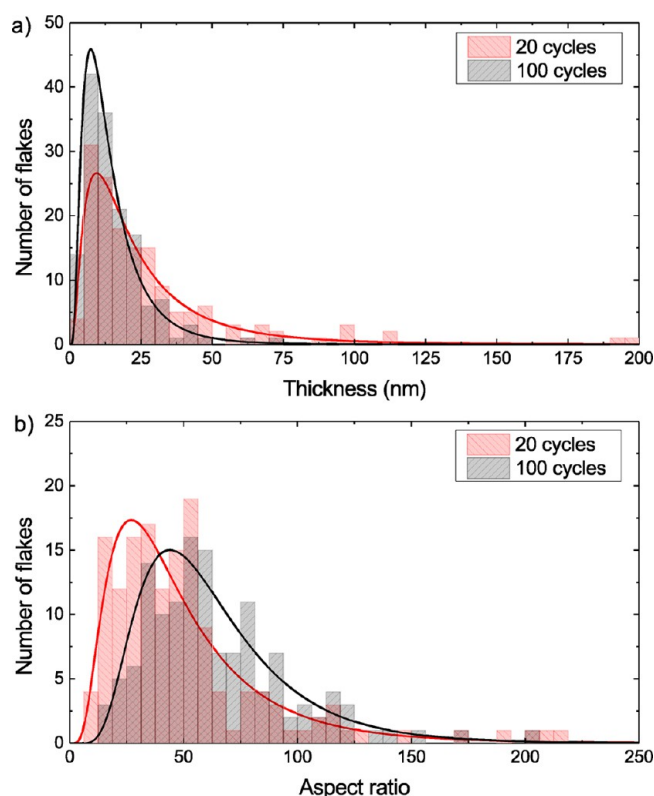

Figure 4. (a) Flake thickness distribution and (b) AR after 20 and 100 cycles, as measured by AFM.

is performed to identify adsorbed or covalently bonded functional groups using a TA Q50 (TA Instruments). Samples are heated from 25 to 100 °C at 10 °C/min and then held isothermally at 100 °C for 10 min to remove residual moisture. T is then ramped up to 1000 °C at a typical heating rate of 10 °C/min.[71] The starting graphite shows ~2 wt % decomposition above 700 °C. Flakes after washing reveal no surfactant, as confirmed by no weight loss at ~400 °C, where SDC suffers significant decomposition, as shown in Figure 6a. However, thermal decomposition of the flakes occurs at ~600 °C, lower than the starting graphite, with a weight loss of ~6 wt %. Flakes with small lateral dimensions and thickness have a lower thermal stability compared to large-area graphitic sheets.[73,74]

The starting graphite and the exfoliated flakes are then fixed onto an adhesive Cu tape for XPS (Escalab 250Xi, Thermo Scientific).[75] The binding energies are adjusted to the sp^2 C$_{1s}$ peak of graphite at 284.5 eV.[76—78] Survey scan spectra (Figure 6b) of the starting graphite and the exfoliated flakes reveal only C$_{1s}$ and O$_{1s}$[76] peaks. The slight increase in oxygen content for the exfoliated flakes compared to the starting material (C$_{1s}$/O$_{1s}$ 35.1 to 25.9) is likely due to the increased ratio of edge to basal plane sites as the flake lateral size decreases. However, C$_{1s}$/O$_{1s}$ remains an order of magnitude larger than the ~3 typically observed in graphene oxide (GO).[79—81] Even following reductive treatments, the C$_{1s}$/O$_{1s}$ ratio in reduced graphene oxide does not exceed ~15,[79,80] i.e., half that measured for our flakes. High-energy resolution (50 eV pass energy) scans are then performed in order to deconvolute the C$_{1s}$ lineshapes. Both the starting graphite and exfoliated flakes can be fitted with 3 components (Figure 6c,d): an asymmetric sp^2 C—C (284.5 eV),[76,78] C—O (~285—286 eV),[78] and π—π* transitions at ~290 eV.[78] Only a slight increase in the relative area of the
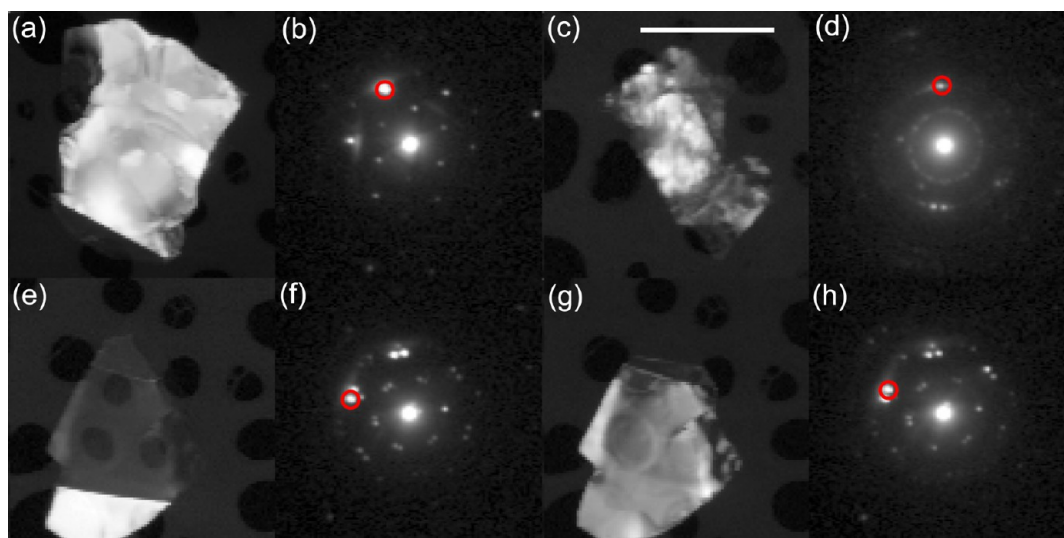
Figure 5. (a,c,e,g) Virtual dark-field images and (b,d,f,h) representative diffraction patterns acquired from (a,b) a single crystal flake, (c,d) a polycrystalline flake, and (e-h) a polycrystalline flake comprising three crystals overlapping one another. The scale bar is 1 μm. Red circles indicate the integration windows used to form the virtual dark-field images.
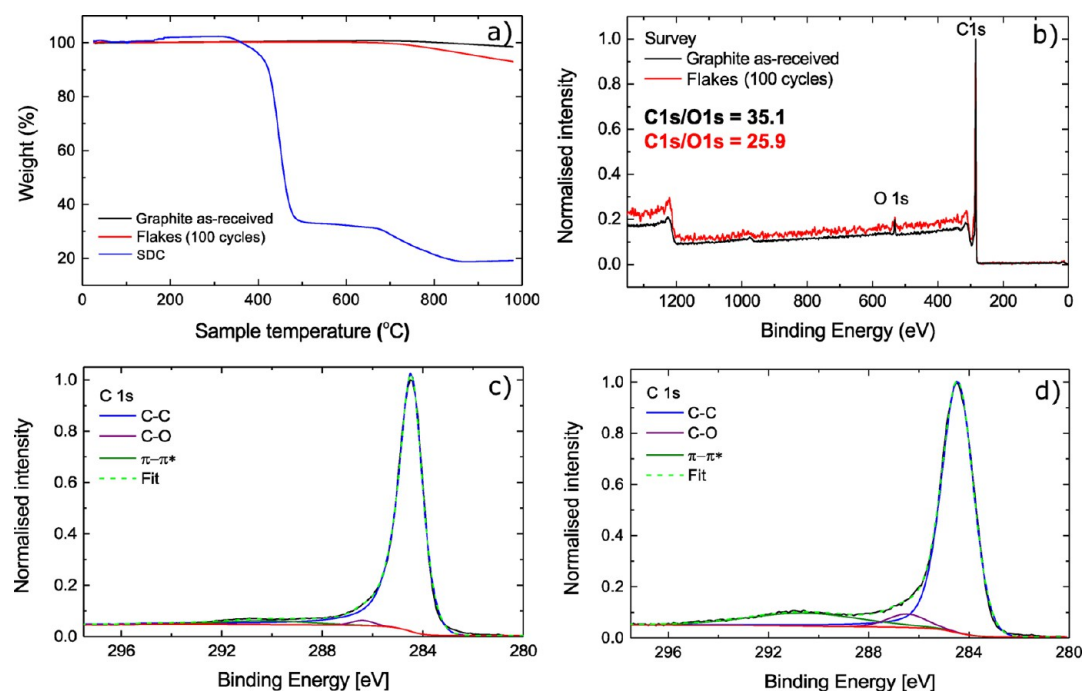

Figure 6. (a) TGA of starting graphite and flakes after 100 cycles and SDC in nitrogen. (b) XPS of starting graphite and after 100 cycles. (c, d) High-resolution C_{1s} spectra of starting graphite and after 100 cycles. Red curves represent the Shirley-type[72] background, which accounts for the effect of the inelastic scattering of electrons.

C−O peak is seen (from ∼2% to ∼5%). Therefore excessive oxidation or additional unwanted chemical functionalizations do not occur during microfluidization.

Raman spectroscopy is then used to assess the structural quality of the flakes. 60 μL of aqueous dispersion is drop cast onto 1 cm × 1 cm Si/SiO$_2$ substrates, then heated at 80−100 °C for 20 min, to ensure water evaporation, and washed with a mixture of water and ethanol (50:50 in volume) to remove SDC. Raman spectra are acquired at 457, 514, and 633 nm using a Renishaw InVia spectrometer equipped with a 50× objective. The power on the sample is kept below 1 mW to avoid any possible damage. The spectral resolution is ∼1 cm^{-1}.

A statistical analysis is performed on the starting graphite and on samples processed for 20, 50, 70, and 100 cycles. The spectra are collected by using a motorized stage as follows: The substrate is divided into 9 equally spaced regions ∼200 × 200 μm^2. In each, 3 points are acquired. This procedure is repeated for each sample and for the 3 wavelengths. The Raman spectrum of graphite has several characteristic peaks. The G peak corresponds to the high-frequency E_{2g} phonon at Γ.[82] The D peak is due to the breathing modes of six-atom rings and requires a defect for its activation.[83] It comes from transverse optical (TO) phonons around the Brillouin zone corner K.[82,83] It is active by double resonance (DR)[84,85] and is strongly
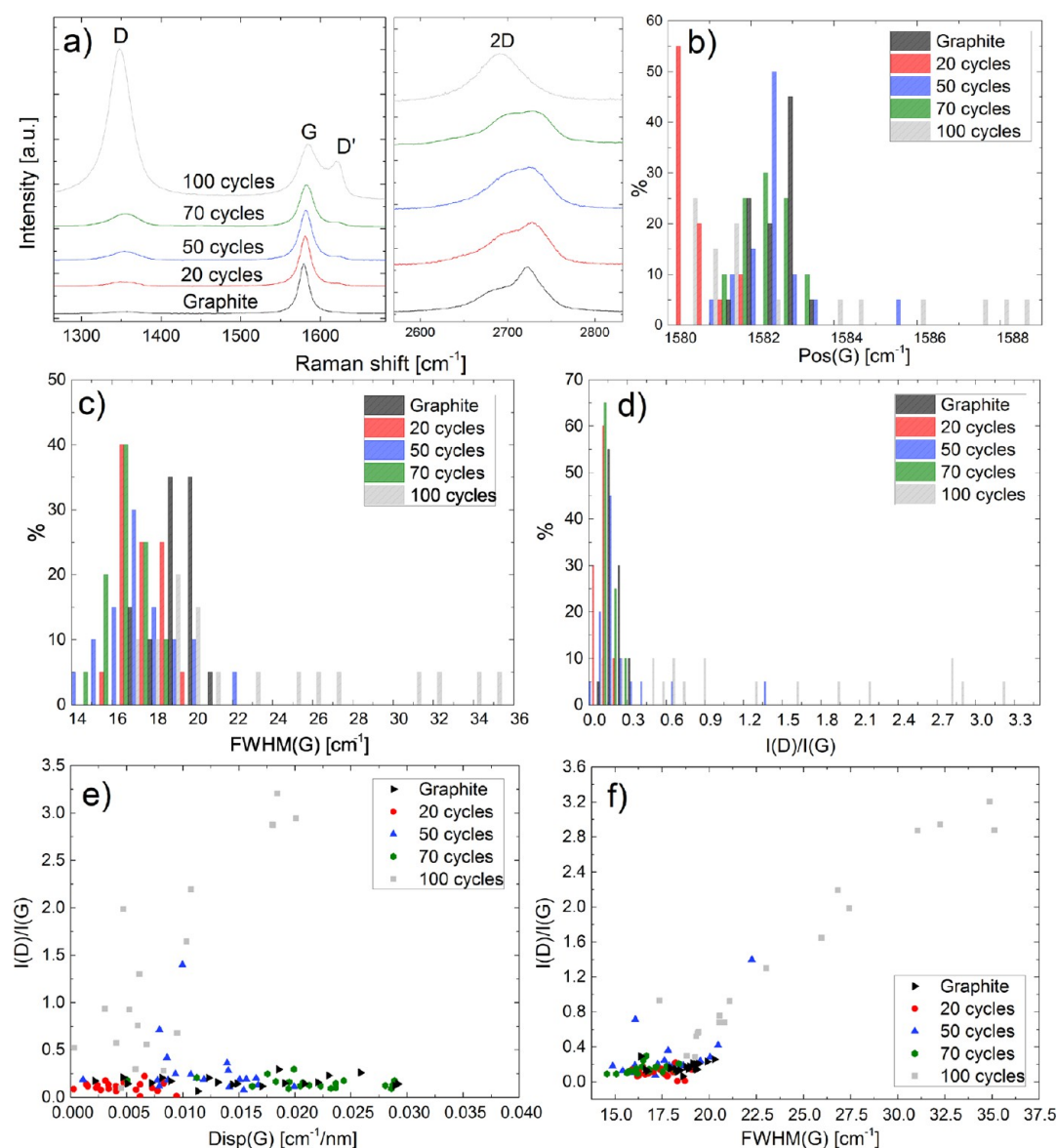
Figure 7. (a) Representative Raman spectra at 514.5 nm for graphite and after 20 (red curve), 50 (blue curve), 70 (green curve), and 100 (gray curve) cycles. (b,c,d) Distribution of (b) Pos(G), (c) FWHM(G) and (d) I(D)/I(G). (e, f) I(D)/I(G) as a function of (e) Disp(G) and (f) FWHM(G).

dispersive with excitation energy[86] due to a Kohn anomaly (KA) at K.[87] DR can also happen as an intravalley process, *i.e.*, connecting two points belonging to the same cone around K (or K′). This gives the so-called D′ peak. The 2D peak is the D peak overtone, and the 2D′ peak is the D′ overtone. Because the 2D and 2D′ peaks originate from a process where momentum conservation is satisfied by two phonons with opposite wave vectors, no defects are required for their activation and are thus always present.[88−90] The 2D peak is a single Lorentzian in SLG, whereas it splits in several components as N increases, reflecting the evolution of the electronic band structure.[88] In bulk graphite, it consists of two components, ∼1/4 and 1/2 the height of the G peak.[88] In disordered carbons, the position of the G peak, Pos(G), increases with decreasing of excitation wavelength (λ_L),[91] resulting in a nonzero G peak dispersion, Disp(G), defined as the rate of change of Pos(G) with excitation wavelength. Disp(G) increases with disorder.[91] Analogously to Disp(G), the full width at half-maximum of the G peak, FWHM(G),

increases with disorder.[92] The analysis of the intensity ratio of the D to G peaks, $I(D)/I(G)$, combined with that of FWHM(G) and Disp(G), allows one to discriminate between disorder localized at the edges and in the bulk. In the latter case, a higher $I(D)/I(G)$ would correspond to higher FWHM(G) and Disp(G). Figure 7a plots representative spectra of the starting graphite (black line) and of flakes after 20 (red line), 50 (blue line), 70 (green line), and 100 cycles (gray line). The 2D band line shape for the starting graphite and the 20−70 cycle samples show two components $(2D_2, 2D_1)$. Their intensity ratio, $I(2D_2)/I(2D_1)$, changes from ∼1.5 for starting graphite to ∼1.2 for 50 and 70 cycles, until the 2D peak becomes a single Lorentzian for 100 cycles, suggesting an evolution to electronically decoupled layers.[90,93] FWHM(2D) for 100 cycles is ∼70 cm^{-1}, significantly larger than in pristine graphene. This implies that, even if the flakes are multilayers, they are electronically decoupled and, to a first approximation, behave as a collection of single layers. Pos(G) (Figure 7b), FWHM(G) (Figure 7c), and $I(D)/I(G)$ (Figure 7d) for 20−70
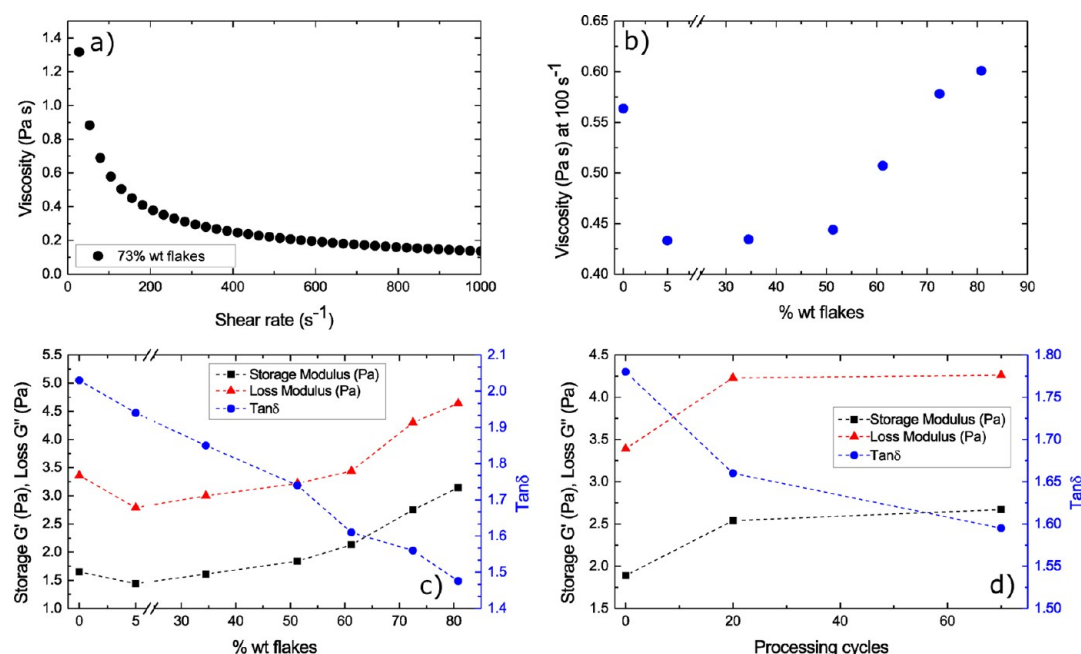
Figure 8. Plots of (a) μ as a function of $\dot{\gamma}$ for an ink with 73 wt % flakes (in the solids content) and (b) μ at 100 s^{-1} for different flakes wt %. (c, d) G', G'', and tan δ as a function of (c) wt % flakes and (d) processing cycles.

cycles do not show a significant difference with respect to the starting graphite. However, for 100 cycles, Pos(G), FWHM(G), and $I(D)/I(G)$ increase up to ~1588 cm^{-1}, 34 cm^{-1}, and 3.2, suggesting a more disordered material. For all the processed samples (20–100), the D peak is present. For 20–70 cycles, it mostly arises from edges, as supported by the absence of correlation between $I(D)/I(G)$, Disp(G) (Figure 7e), and FWHM(G) (Figure 7f). The correlation between $I(D)/I(G)$, Disp(G) (Figure 7e), and FWHM(G) (Figure 7f) for 100 cycles indicates that D peak arises not only from edges but also from in-plane defects. Therefore, we select 70 cycles to formulate conductive printable inks. We note that here we use synthetic microcrystalline graphite flakes instead of large natural or single crystal flakes sometimes used by other LPE-based works.[37,52,55,94,95] Our flakes produced up to 70 cycles are of comparable quality, as shown by Raman spectroscopy.

Printable Inks Formulation. Following microfluidization, carboxymethylcellulose sodium salt (CMC) (weight-average molecular weight, M_W = 700.000, Aldrich no. 419338), a biopolymer[96] which is a rheology modifier,[97,98] is added to the dispersion to stabilize the flakes against sedimentation. CMC is added at C = 10 g/L over a period of 3 h at room temperature. This is necessary because if all of the CMC is added at once, aggregation occurs, and these aggregates are very difficult to dissolve. The mixture is continuously stirred until complete dissolution. Different inks are prepared, keeping constant the SDC C = 9 g/L and CMC C = 10 g/L, while increasing the flakes C to 1, 10, 20, 30, 50, 80, and 100 g/L. Once printed and dried, these formulations correspond to 5, 35, 51, 61, 73, 81, and 84 wt % of flakes in the total solids content, respectively.

The rheological properties are investigated using a Discovery HR-1 rheometer (TA Instruments) in a parallel-plate (40 mm diameter) configuration.[99] We monitor the elastic modulus G' [J/m^3 = Pa], representing the energy density stored by the material under shear,[100] and the loss modulus G'' [J/m^3 = Pa],[100] representing the energy density lost during a shear process due to friction and internal motions.[100] Flow curves are

measured by increasing $\dot{\gamma}$ from 1 to 1000 s^{-1} at a gap of 0.5 mm, because this $\dot{\gamma}$ range is applied during screen printing.[101] Figure 8a plots the steady-state μ of an ink containing 73 wt % flakes (70 cycles) as a function of $\dot{\gamma}$. CMC imparts a drop in μ under shear, from 570 mPa·s at 100 s^{-1} to 140 mPa·s at 1000 s^{-1}. This is a thixotropic behavior,[102] since the μ reduces with $\dot{\gamma}$. The higher $\dot{\gamma}$, the lower μ.[102] This behavior is shown by some non-Newtonian fluids, such as polymer solutions[103] and biological fluids.[104] It is caused by the disentanglement of polymer coils or by the increased orientation of polymer coils in the direction of the flow.[102] On the other hand, in Newtonian liquids the viscosity does not change with $\dot{\gamma}$.[104] Refs 105 and 106 reported that thixotropy in CMC solutions arises from the presence of unsubstituted (free) OH groups. Thixotropy increases as the number of OH groups increases.[105,106]

During printing, shear is applied to the ink, and its μ decreases, making the ink easier to print or coat. This shear thinning behavior facilitates the use of the ink in techniques such as screen printing, in which a maximum $\dot{\gamma} \sim 1000$ s^{-1} is reached when the ink penetrates the screen mesh.[101] Figure 8b plots μ at 100 s^{-1} as a function of wt % flakes (70 process cycles). The CMC polymer (10 g/L in water) has $\mu \sim 0.56$ Pa·s at 100 s^{-1} and drops to 0.43 Pa·s for C = 1 g/L, i.e. 5 wt % flakes in the solids content. The flakes wt % affects μ, which reaches 0.6 Pa·s at 80 wt %.

More information on the ink rheological behavior and microstructure can be obtained by oscillatory rheology measurements.[107] CMC gives a viscoelastic character to the ink. This can also be evaluated in terms of the loss factor, defined as tan $\delta = G''/G'$.[100] The lower tan δ, the more solid-like (i.e., elastic) the material is at a given strain or frequency.[100] Figure 8c plots G', G'', and tan δ at 1% strain, checked from dynamic amplitude sweeps in order to be within the linear viscoelastic region (LVR). In LVR, G' and G'' are not stress or strain dependent[108] as a function of flake loading. The addition of 5 wt % flakes in CMC decreases both G' and G'', which start
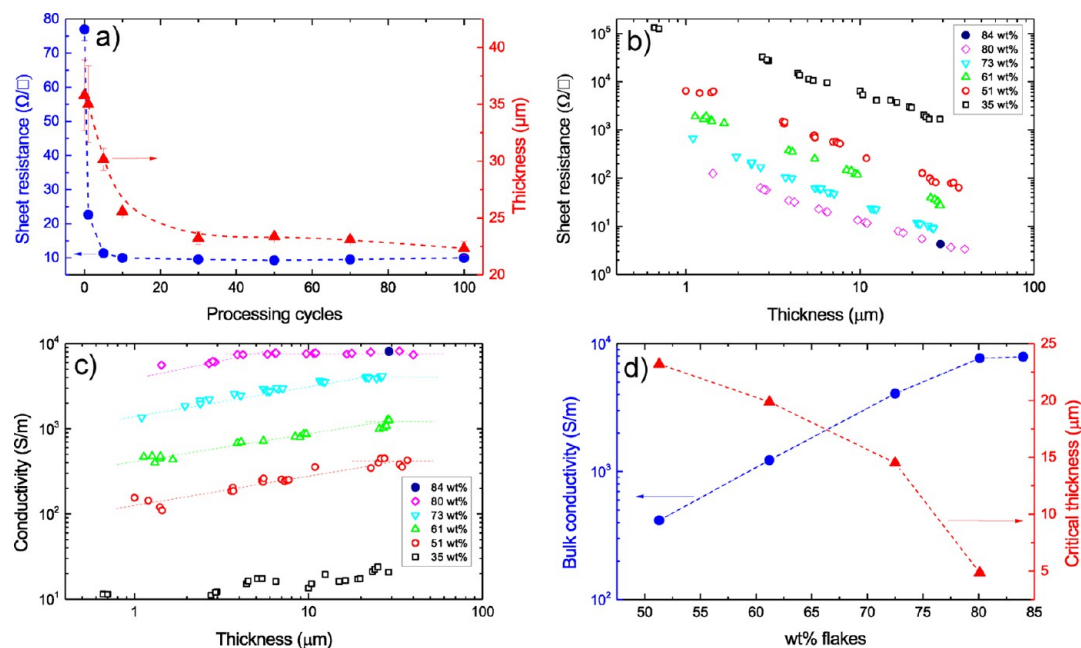
Figure 9. (a) R_s and h as a function of processing cycles for a formulation with ~73 wt % flakes. (b) R_s as a function of h for different wt % (70 cycles). (c) σ as a function of h for different wt %. (d) Bulk σ and critical h as a function of wt % (70 cycles). All samples are dried for 10 min at 100 °C.

to increase for loadings above 30 wt %. Tan δ decreases with flake loading, leading to a more solid-like behavior. We estimate G', G'', and tan δ also for inks containing flakes processed at different cycles, while keeping the flakes loading at ~73%, Figure 8d. Both G' and G'' increase with processing cycles, while tan δ decreases, indicating an increase of elastic behavior with processing.

For simplicity, blade coating is used to compare ink formulations. Inks are blade coated onto glass microscope slides (25×75 mm) using a spacer to control h. The films are dried at 100 °C for 10 min to remove water. The h depends on the wet film thickness, the total solid content wt % of the ink, and the number of processing cycles. We investigate the effects of processing cycles, flake content, and postdeposition annealing on R_s. This is measured in four different locations per sample using a four-point probe. A profilometer (DektakXT, Bruker) is used to determine h for each point. In order to test the effect of the processing cycles, films are prepared from inks containing ~73 wt % flakes processed for 0, 5, 10, 30, 50, 70, and 100 cycles keeping the wet h constant (1 mm). Figure 9a shows the effect of processing cycles on R_s and h. Without any processing, the films have $R_s \sim 77\,\Omega/\square$ and $h = 35.8$ μm, corresponding to $\sigma \sim 3.6 \times 10^2$ S/m. Microfluidization causes a drop in R_s and h. Ten cycles are enough to reach ~$10\,\Omega/\square$ and $h \sim 25.6$ μm, corresponding to $\sigma \sim 3.9 \times 10^3$ S/m. R_s does not change significantly between 10 and 100 cycles, while h slightly decreases. We get $\sigma \sim 4.5 \times 10^2$ S/m above 30 cycles.

The effect of flake loading for a fixed number of processing cycles (70) is investigated as follows. Dispersions with different loadings are prepared by increasing the flakes C between 1 and 100g/L, while keeping the SDC (9g/L) and CMC (10g/L) constant. Films of different h are prepared by changing the spacer height during blade coating, leading to different wet and dry h. R_s and σ as a function of h are shown in Figures 9b,c. At ~ 34.5 wt % the flakes already form a percolative network

within the CMC matrix, and $\sigma \sim 15-20$ S/m is achieved (σ of cellulose derivative films is $<10^{-8}$ S/m).[109] Figure 9c shows that, for a given composition, there is a critical h below which σ is thickness dependent. Above this, the bulk σ is reached. As shown in Figure 9c, for ~80 wt % we get $\sigma \sim 7.7 \times 10^3$ S/m for $h > 4.5$ μm. Higher loadings (84 wt %) do not increase σ further. Figure 9d indicates that the critical h, where the bulk σ is reached, drops from ~20 μm for 51 wt % to ~4.5 μm for 80 wt %. Coatings with $h > 4.5$ μm can be easily achieved using screen printing in a single printing pass. Figure 9c shows that σ is h dependent up to a critical point. In order to understand the effect of h on σ, we adapt the percolation model of ref 110. The total area covered by nonoverlapping flakes is A_f (e.g., for elliptical flakes $A_f = m\pi ab$, where m is the number of flakes and a [m] and b [m] are their half axes lengths). The fractional area covered by the (overlapping) flakes, with respect to the total area S [m^2], can be evaluated as $q = 1 - p$, with $p = e^{-A_f/S}$, where q is the fractional area covered by the flakes;[110] q coincides with A_f/S only when the flakes do not overlap. Denoting by $A_f h_f$ the total flakes volume and f the volume fraction of flakes in the films we have

$$A_f h_f = fhS = -Sh_f \ln p \qquad (1)$$

and σ follows a power law behavior[110]:

$$\sigma = k(q - q_c)^n \qquad (2)$$

around the percolation threshold q_c,[110] with n as the electrical conductivity critical exponent above percolation. Eqs 1 and 2 give

$$\sigma = \sigma_\infty [1 - e^{(h_c - h)f/h_f}]^n \qquad (3)$$

where $\sigma_\infty = ke^{(-fnh_c/h_f)}$ and h_c is the critical thickness corresponding to zero σ. As a function of h, σ is fitted with eq 3 in Figure 10 for ~73 wt %, i.e., $f = 0.61$, giving $\sigma_\infty \sim 4.3 \times 10^3$ S/m, $h_c = 0.39$ μm, $h_f \sim 7.58$ μm, and $n = 0.39$.
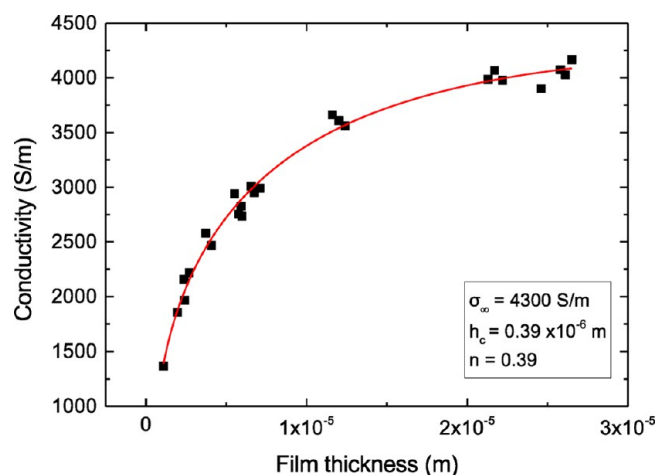
Figure 10. Fit of σ as a function of h according to eq 3 for 73 wt % of flakes in the film.
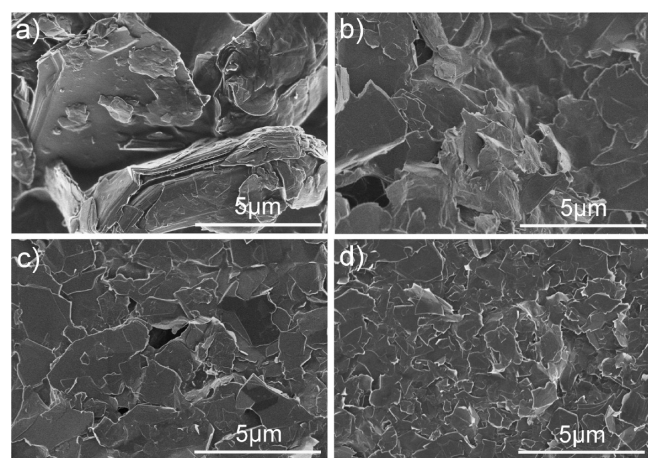

Figure 11. SEM images taken from coatings comprising (a) starting graphite, (b) after 1 cycle, (c) after 5 cycles, and (d) after 100 cycles. The scale bar is 5 μm.
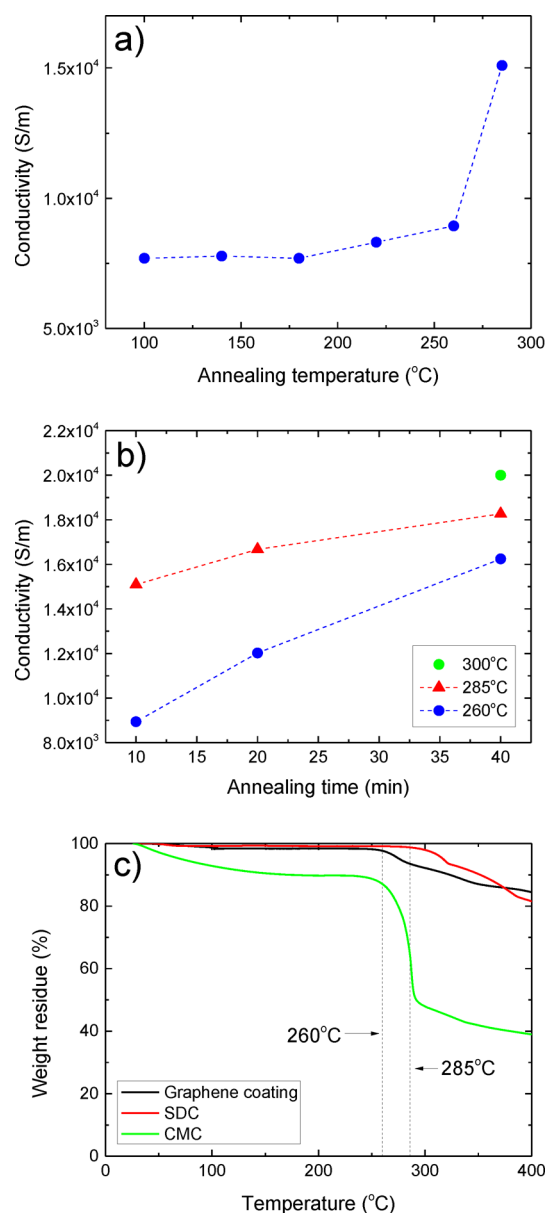

Figure 12. Plots of σ as a function of (a) T and (b) time. (c) TGA thermograms from coatings compared with the SDC (powder) and the CMC (powder) components.

Figure 11 shows SEM images of the coatings comprising the starting graphite (Figure 11a) and after 1 (Figure 11b), 5 (Figure 11c), and 100 cycles (Figure 11d). Flake size reduction and platelet-like morphology are observed after the first cycle, Figure 11b. The samples have fewer voids compared to the starting graphite, providing higher interparticle contact area and higher packing density, consistent with the h reduction (Figure 9a) and the increased σ. While the packing density increase results in more pathways for conduction, the smaller flake size increases the number of interparticle contacts. Then, R_s remains constant.

Postdeposition annealing is studied in blade-coated films for ~80 wt % flakes after 70 cycles. Figure 12a plots σ as a function of T. A three-step regime can be seen. In the first (100−180 °C), σ is constant (~7.7 × 10³ S/m), and above 180 °C, it increases, reaching 9 × 10³ S/m at 260 °C, followed by a significant increase at 285 °C to ~1.5 × 10⁴ S/m. Figure 12b shows the effect of annealing time at 260, 285, or 300 °C. Either higher T or longer annealing times are required to increase σ.

TGA is then used to investigate the thermal stability of the films (Figure 12c). The thermogram of the CMC polymer reveals a 10% weight loss up to 200 °C, due to water loss.[111]

Figure 12 also shows that 50% of the CMC is decomposed at 285 °C, while the SDC surfactant remains intact. Annealing at 300 °C for 40 min leads to films with R_s ~ 2Ω/□ (25 μm), corresponding to σ ~ 2 × 10⁴ S/m. This σ is remarkable, given the absence of centrifugation, usually performed to remove the nonexfoliated material, or washing steps to remove the nonconductive polymer and surfactant materials. The SDC additive stabilizes the flakes against restacking through electrostatic repulsion, forming a large contact area per surfactant molecule.[40] CMC further stabilizes against restacking through electrosteric repulsion.[112] Thus, R_s of our patterns is <2Ω/□, surpassing other reported printable graphene inks.[94,113−115] Our inks also could be exploited to prepare transparent conductive films, by using grids, e.g., a grid with line width ~100 μm and a pitch distance ~2000 μm would give ~90% transparency, combined with low R_s ~ 100Ω/□ at a thickness of 10 μm.

The printability of the ink with ~80 wt % flakes after 70 cycles is tested using a semiautomatic flatbed screen printer (Kippax kpx 2012) and a Natgraph screen printer (Figure 13a), both equipped with screens with 120 mesh count per inch. Figure 13b shows a 29 × 29 cm^2 print on paper with a line resolution ~100 μm (Figure 13c). The pattern (Figure 13b) can be used as a capacitive touch pad in a sound platform that translates touch into audio.[116] The electronic module has a series of 12 contact pads (2.5 cm × 2.5 cm) on its underside

Figure 13. (a) Demonstration of screen printing, (b) capacitive touchpad design (29 cm × 29 cm) printed on paper, and (c) the line resolution is 100 μm.

that are interfaced to printed electronic pads on the paper surface. This maintains a set-point charge on each of the printed capacitive touch pads. When a touch-pad is touched, it undergoes an instantaneous discharge that is then identified by the electronics, and a corresponding sound is played. We measured the normalized resistance (resistance after bending/resistance prior to bending) for up to 1400 cycles for a bending radius of 12.5 mm and observed a change <1%.

CONCLUSION

We report a simple and scalable route to exfoliate graphite. The resulting material can be used without any additional steps (washing or centrifugation) to formulate highly conductive inks with adjustable viscosity for high-throughput printing. A conductivity of 2 × 10^4 S/m was demonstrated. Our approach enables the mass production of chemically unmodified flakes that can be used in inks, coatings, and conductive composites for a wide range of applications.

METHODS

Microfluidization Process. In order to compare the microfluidization process with sonication or shear mixing, it is important to elucidate its fluid dynamics. The mean velocity U [m/s] of the fluid inside the microchannel is[117]

$$U = \frac{Q}{A} \tag{4}$$

where Q [m^3/s] is the volumetric flow rate, defined as[118]

$$Q = \frac{c_n V}{t} \tag{5}$$

where c_n is the number of cycles, V [m^3] the volume of material (graphite and solvent) passing a point per unit time t [s], and A [m^2] is the channel cross-sectional area, given by

$$A = \pi \left(\frac{D_h}{2}\right)^2 \tag{6}$$

where $D_h = 4A/P$ is the hydraulic diameter of the microchannel, with P the wetted perimeter (i.e., the part of the microchannel in contact with the flowing fluid[117]). For a batch of 0.18 L, it takes 1.93 h to complete 70 cycles. Eq 5 gives $Q = 1.8 \times 10^{-6}$ m^3/s. Eq 6 with $D_h \sim 87$ μm[58] gives $A = 5940 \times 10^{-12}$ m^2. Then, from eq 4 we get $U \sim 304$m/s.

The Reynolds number, Re, can be used to determine the type of flow, and it is given by[117]

$$Re = \frac{\rho U D_h}{\mu} \tag{7}$$

where ρ [kg/m^3] is the liquid density. We typically use 50 up to 100 g/L of graphite, which corresponds to a total density (mixture of graphite and water) of 1026−1052 kg/m^3; μ [Pa·s] is the (dynamic) viscosity ($\mu = \tau/\dot{\gamma}$, where τ [Pa] is the shear stress). We measure μ with a rotational rheometer in which a known $\dot{\gamma}$ is applied to the sample, and the resultant torque (or τ) is measured.[99] We get $\mu \sim 1 \times 10^{-3}$ Pa·s (20 °C), similar to water.[117] Thus, eq 7 gives $Re \sim 2.7 \times 10^4$, which indicates that there is a fully developed turbulent flow inside the microchannel (there is a transition from laminar to turbulent flow in the 2000 > Re > 4000 range).[119]

The pressure losses inside the channel can be estimated by the Darcy−Weisbach equation,[117] which relates the pressure drop, due to friction along a given length of pipe, to the average velocity of the fluid flow for an incompressible fluid:[117]

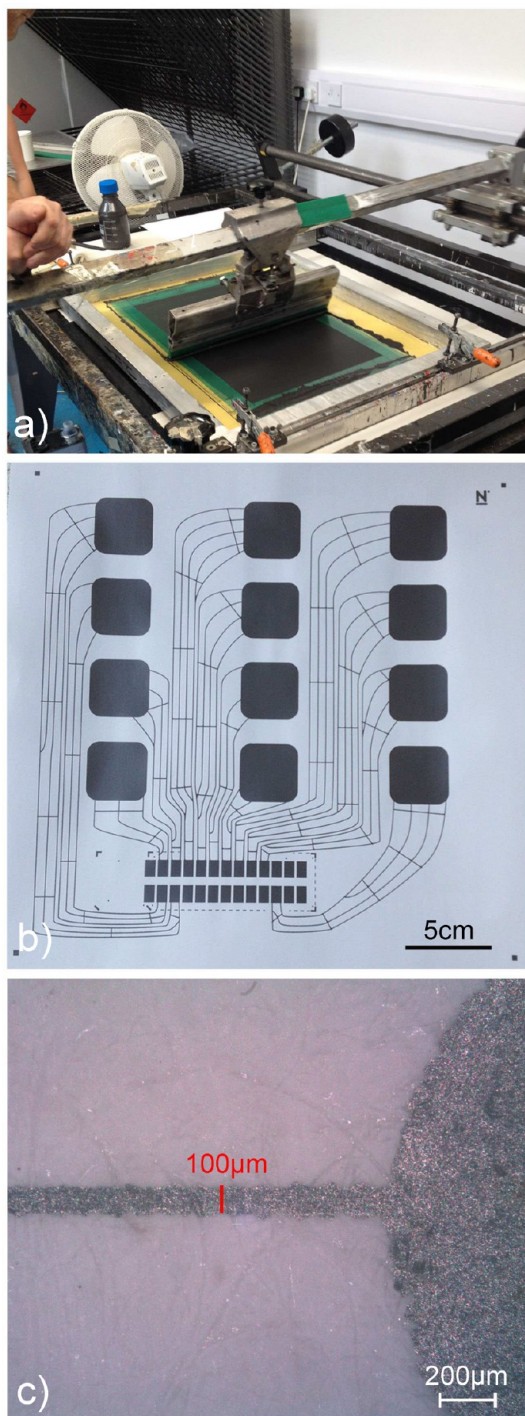$$\Delta p = \frac{f_D L \rho U^2}{2 D_h} \tag{8}$$

where Δp [Pa] is the pressure drop, L [m] is the pipe length, and f_D is the Darcy friction factor, a dimensionless quantity used for the description of friction losses in pipe flow.[117] The energy dissipation rate per unit mass ε [m²/s³] inside the channel can be written as[120]

$$\varepsilon = \frac{Q\,\Delta p}{\rho V_c} \tag{9}$$

where V_c is the volume of the liquid inside the microchannel. From eqs 8 and 9, we can rewrite ε as

$$\varepsilon = \frac{f_D U^3}{2 D_h} \tag{10}$$

For $Re = 2.7 \times 10^4$, we get $f_D \sim 0.052$ from the Moody chart,[121] which links f_D, Re, and the relative roughness of the pipe (= absolute roughness/hydraulic diameter[117]). From eqs 4, 5, 6, and 10, we get $\varepsilon \sim 8.5 \times 10^9$ m²/s³, and $\dot\gamma$ can then be estimated as[122]

$$\dot\gamma = \sqrt{\frac{\varepsilon}{\nu}} \tag{11}$$

where ν [m²/s] is the kinematic viscosity,[122] defined as $\nu = \mu/\rho \sim 1 \times 10^{-6}$ m²/s. From eq 11, we get $\dot\gamma \sim 10^8$ s⁻¹, which is 4 orders of magnitude higher than that required to initiate graphite exfoliation.[52] Then, the exfoliation in the microfluidizer is primarily due to shear stress generated by the turbulent flow. In comparison, in a rotor-stator shear mixer, lower $\dot\gamma \sim 2 \times 10^4$ to 1×10^5 s⁻¹ are achieved[54,122,123] and only near the probe.[54] Thus, exfoliation does not take place in the entire batch uniformly.[52] On the contrary, in a microfluidizer all the material is uniformly exposed to high shear forces.[62]

Turbulent mixing is characterized by a near dissipationless cascade of energy,[122] i.e., the energy is transferred from large (on the order of the size of the flow geometry considered) random, three-dimensional eddy-type motions to smaller ones (on the order of the size of a fluid particle).[117] This takes place from the inertial subrange (IS) of turbulence where inertial stresses dominate over viscous stresses, down to the Kolmogorov length,[124] η [m], i.e., the length-scale above which the system is in the IS and below which it is in the viscous subrange (VS), where turbulence energy is dissipated by heat,[122,125] and η can be calculated as[124]

$$\eta = \left(\frac{\nu^3}{\varepsilon}\right)^{1/4} \tag{12}$$

From $\nu \sim 1 \times 10^{-6}$ m²/s and eq 9, we get $\eta \sim 103$ nm for microfluidization in water. Since our starting graphitic particles are much larger (>μm) than η, exfoliation occurs in the IS rather than VS. In comparison, in a kitchen blender $\eta = 6$ μm,[126] thus exfoliation occurs in the VS, i.e., the energy is dissipated through viscous losses, rather than through particle disruption. During microfluidization, in the IS, the main stress contributing to exfoliation is due to pressure fluctuations, i.e., the graphite is bombarded with turbulent eddies. This stress, τ_{IS} [Pa], can be estimated as[122]

$$\tau_{IS} \sim \rho (\varepsilon d_g)^{2/3} \tag{13}$$

where d_g is the diameter of a sphere of equivalent volume to the flakes. For $d_g = 0.1$ to 27 μm, τ_{IS} is in the ~0.1−4 MPa range. The dynamic pressure also breaks the flakes as well as exfoliating them. For length scales <η, we are in the VS, and the stress applied on the fakes, τ_{VS}, can be estimated as[122]

$$\tau_{VS} \sim \mu \sqrt{\frac{\varepsilon}{\nu}} \tag{14}$$

which gives $\tau_{VS} \sim 0.1$ MPa. Thus, the stresses applied on the flakes in the IS are much higher than in the VS, where energy is lost by heat. This can lead to more defects in the basal plane. The Kolmogorov length can be tuned, eq 12, by either increasing the kinematic viscosity of the dispersion or decreasing the energy dissipation rate, thus extending the viscous subrange of turbulence realizing a milder exfoliation.

In microfluidization, the energy density, E/V [J/m³], (where E [J] is the energy) equates the pressure differential,[61] due to very short residence times ~10^{-4} s,[61] i.e., the time the liquid spends in the microchannel. Therefore, for a processing pressure ~207 MPa, $E/V = 207$ MPa = 2.07×10^8 J/m³. For this total energy input per unit volume, the flakes production rate $P_r = VC/t$ [g/h] for a typical batch of $V = 0.18$ L and $t = 1.93$h (for 70 cycles) is $P_r \sim 9.3$ g/h, with starting graphite concentration ~100 g/L using a lab-scale system. Scale-up can be achieved by increasing Q, using a number of parallel microchannels,[58] which decreases the time required to process a given V and c_n (eq 5). With shorter time, P_r increases. Large-scale microfluidizers can achieve flow rates ~12 L/min[58] at processing pressure ~207 MPa, which correspond to $P_r = CQ/c_n \sim 1$ kg/h (~9 ton per year, ~90,000 L of ink per year) in an industrial system using 70 process cycles and $C = 100$ g/L.

AUTHOR INFORMATION

Corresponding Author
*E-mail: acf26@eng.cam.ac.uk.

ORCID
Duncan N. Johnstone: 0000-0003-3663-3793
Andrea C. Ferrari: 0000-0003-0907-9993

Notes
The authors declare no competing financial interest.

REFERENCES

(1) Jung, S.; Hoath, S. D.; Martin, G. D.; Hutchings, I. M. Inkjet Printing Process for Large Area Electronics. In Large Area and Flexible Electronics; Caironi, M., Noh, Y.-Y., Eds; Wiley-VCH Verlag GmbH & Co. KGaA: Weinheim, Germany, 2015; pp 317−341.

(2) Leppäniemi, J.; Huttunen, O.-H.; Majumdar, H.; Alastalo, A. Flexography-Printed In2O3 Semiconductor Layers for High-Mobility Thin-Film Transistors on Flexible Plastic Substrate. Adv. Mater. 2015, 27, 7168−7175.

(3) Lau, P. H.; Takei, K.; Wang, C.; Ju, Y.; Kim, J.; Yu, Z.; Takahashi, T.; Cho, G.; Javey, A. Fully Printed, High Performance Carbon Nanotube Thin-Film Transistors on Flexible Substrates. Nano Lett. 2013, 13, 3864−3869.

(4) Krebs, F. C.; Fyenbo, J.; Jørgensen, M. Product Integration of Compact Roll-to-Roll Processed Polymer Solar Cell Modules: Methods and Manufacture using Flexographic Printing, Slot-die Coating and Rotary Screen Printing. J. Mater. Chem. 2010, 20, 8994−9001.

(5) Dearden, A. L.; Smith, P. J.; Shin, D.-Y.; Reis, N.; Derby, B.; O'Brien, P. A Low Curing Temperature Silver Ink for Use in Ink-Jet Printing and Subsequent Production of Conductive Tracks. Macromol. Rapid Commun. 2005, 26, 315−318.

(6) Magdassi, S.; Grouchko, M.; Kamyshny, A. Copper Nanoparticles for Printed Electronics: Routes Towards Achieving Oxidation Stability. Materials 2010, 3, 4626−4638.

(7) Wang, J.; Pamidi, P. V. A. Sol-Gel-Derived Gold Composite Electrodes. Anal. Chem. 1997, 69, 4490−4494.

(8) Jeong, S.; Woo, K.; Kim, D.; Lim, S.; Kim, J. S.; Shin, H.; Xia, Y.; Moon, J. Controlling the Thickness of the Surface Oxide Layer on Cu

Nanoparticles for the Fabrication of Conductive Structures by Ink-Jet Printing. *Adv. Funct. Mater.* **2008**, *18*, 679−686.

(9) Grouchko, M.; Kamyshny, A.; Mihailescu, C. F.; Anghel, D. F.; Magdassi, S. Conductive Inks with a "Built-In" Mechanism That Enables Sintering at Room Temperature. *ACS Nano* **2011**, *5*, 3354−3359.

(10) Rida, A.; Yang, L.; Vyas, R.; Tentzeris, M. M. Conductive Inkjet-Printed Antennas on Flexible Low-Cost Paper-Based Substrates for RFID and WSN Applications. *IEEE Antennas Propag. Mag.* **2009**, *51*, 13−23.

(11) Kim, Y.; Lee, B.; Yang, S.; Byun, I.; Jeong, I.; Cho, S. M. Use of Copper Ink for Fabricating Conductive Electrodes and RFID Antenna Tags by Screen Printing. *Curr. Appl. Phys.* **2012**, *12*, 473−478.

(12) Lucera, L.; Kubis, P.; Fecher, F. W.; Bronnbauer, C.; Turbiez, M.; Forberich, K.; Ameri, T.; Egelhaaf, H.-J.; Brabec, C. J. Guidelines for Closing the Efficiency Gap between Hero Solar Cells and Roll-To-Roll Printed Modules. *Energy Technol.* **2015**, *3*, 373−384.

(13) Huang, X.; Leng, T.; Zhang, X.; Chen, J. C.; Chang, K. H.; Geim, A. K.; Novoselov, K. S.; Hu, Z. Binder-free Highly Conductive Graphene Laminate for Low Cost Printed Radio Frequency Applications. *Appl. Phys. Lett.* **2015**, *106*, 203105.

(14) Hösel, M.; Søndergaard, R. R.; Angmo, D.; Krebs, F. C. Comparison of Fast Roll-to-Roll Flexographic, Inkjet, Flatbed, and Rotary Screen Printing of Metal Back Electrodes for Polymer Solar Cells. *Adv. Eng. Mater.* **2013**, *15*, 995−1001.

(15) Sommer-Larsen, P.; Jørgensen, M.; Søndergaard, R. R.; Hösel, M.; Krebs, F. C. It is all in the Pattern-High-Efficiency Power Extraction from Polymer Solar Cells through High-Voltage Serial Connection. *Energy Technol.* **2013**, *1*, 15−19.

(16) Krebs, F. C.; Espinosa, N.; Hösel, M.; Søndergaard, R. R.; Jørgensen, M. 25th Anniversary Article: Rise to Power - OPV-Based Solar Parks. *Adv. Mater.* **2014**, *26*, 29−39.

(17) Barker, M. J. Screen inks. In *The Printing Ink Manual*, Leach, R. H., Pierce, R. J., Hickman, E. P., Mackenzie, M. J., Smith, H. G., Eds.; Springer: Amsterdam, The Netherlands, 2007; pp 599−634.

(18) Khan, S.; Lorenzelli, L.; Dahiya, R. S. Technologies for Printing Sensors and Electronics Over Large Flexible Substrates: A Review. *IEEE Sens. J.* **2015**, *15*, 3164−3185.

(19) Tobjörk, D.; Österbacka, R. Paper Electronics. *Adv. Mater.* **2011**, *23*, 1935−1961.

(20) Merilampi, S.; Laine-Ma, T.; Ruuskanen, P. The Characterization of Electrically Conductive Silver Ink Patterns on Flexible Substrates. *Microelectron. Reliab.* **2009**, *49*, 782−790.

(21) Hyun, W. J.; Lim, S.; Ahn, B. Y.; Lewis, J. A.; Frisbie, C. D.; Francis, L. F. Screen Printing of Highly Loaded Silver Inks on Plastic Substrates Using Silicon Stencils. *ACS Appl. Mater. Interfaces* **2015**, *7*, 12619−12624.

(22) *Silverprice*. http://silverprice.org (accessed November 7, 2016).

(23) *Infomine*. http://infomine.com/investment/metal-prices/copper/5-year/ (accessed November 7, 2016).

(24) Kamyshny, A.; Magdassi, S. Conductive Nanomaterials for Printed Electronics. *Small* **2014**, *10*, 3515−3535.

(25) Lachkar, A.; Selmani, A.; Sacher, E.; Leclerc, M.; Mokhliss, R. Metallization of Polythiophenes I. Interaction of Vapor-Deposited Cu, Ag and Au with Poly(3- hexylthiophene) (P3HT). *Synth. Met.* **1994**, *66*, 209−215.

(26) Zhang, H. X-ray Microbeam Analysis of Electromigration in Copper Interconnects. In *Electromigration in thin films and electronic devices, Materials and reliability*; Kim, C.-U., Ed.; Woodhead Publishing Limited: Cambridge, U.K., 2011; pp 97−110.

(27) Rösch, R.; Tanenbaum, D. M.; Jørgensen, M.; Seeland, M.; Bärenklau, M.; Hermenau, M.; Voroshazi, E.; Lloyd, M. T.; Galagan, Y.; Zimmermann, B.; Würfel, U.; Hösel, M.; Dam, H. F.; Gevorgyan, S. A.; Kudret, S.; Maes, W.; Lutsen, L.; Vanderzande, D.; Andriessen, R.; Teran-Escobar, G.; et al. Investigation of the Degradation Mechanisms of a Variety of Organic Photovoltaic Devices by Combination of Imaging techniques-the ISOS-3 Inter-laboratory Collaboration. *Energy Environ. Sci.* **2012**, *5*, 6521−6540.

(28) Søndergaard, R. R.; Espinosa, N.; Jørgensen, M.; Krebs, F. C. Efficient Decommissioning and Recycling of Polymer Solar Cells: justification for use of silver. *Energy Environ. Sci.* **2014**, *7*, 1006−1012.

(29) Fahmy, B.; Cormier, S. A. Copper Oxide Nanoparticles Induce Oxidative Stress and Cytotoxicity in Airway Epithelial Cells. *Toxicol. In Vitro* **2009**, *23*, 1365−1371.

(30) Ahamed, M.; Siddiqui, M. A.; Akhtar, M. J.; Ahmad, I.; Pant, A. B.; Alhadlaq, H. A. Genotoxic Potential of Copper Oxide Nanoparticles in Human Lung Epithelial Cells. *Biochem. Biophys. Res. Commun.* **2010**, *396*, 578−583.

(31) Karlsson, H. L.; Cronholm, P.; Gustafsson, J.; Möller, L. Copper Oxide Nanoparticles Are Highly Toxic: A Comparison between Metal Oxide Nanoparticles and Carbon Nanotubes. *Chem. Res. Toxicol.* **2008**, *21*, 1726−1732.

(32) *Statista*. http://statista.com (accessed November 7, 2016).

(33) *Conductive Carbon Ink C2130925D1*. http://gwent.org (accessed November 7, 2016).

(34) *Low-resistivity, screen-printable, carbon ink, LOCTITE EDAG PF 407C E&C*. http://henkel-adhesives.com/ (accessed November 7, 2016).

(35) *DuPont 7102 and BQ242 Conductive Carbon Inks*. http://dupont.com (accessed November 7, 2016).

(36) Ferrari, A. C.; Bonaccorso, F.; Fal'ko, V.; Novoselov, K. S.; Roche, S.; Bøggild, P.; Borini, S.; Koppens, F. H. L.; Palermo, V.; Pugno, N.; Garrido, J. A.; Sordan, R.; Bianco, A.; Ballerini, L.; Prato, M.; Lidorikis, E.; Kivioja, J.; Marinelli, C.; Ryhänen, T.; Morpurgo, A.; et al. Science and Technology Roadmap for Graphene, Related Two-dimensional Crystals, and Hybrid Systems. *Nanoscale* **2015**, *7*, 4598−4810.

(37) Hernandez, Y.; Nicolosi, V.; Lotya, M.; Blighe, F. M.; Sun, Z.; De, S.; McGovern, I. T.; Holland, B.; Byrne, M.; Gun'Ko, Y. K.; Boland, J. J.; Niraj, P.; Duesberg, G.; Krishnamurthy, S.; Goodhue, R.; Hutchison, J.; Scardaci, V.; Ferrari, A. C.; Coleman, J. N. High-Yield Production of Graphene by Liquid-Phase Exfoliation of Graphite. *Nat. Nanotechnol.* **2008**, *3*, 563−568.

(38) Vallés, C.; Drummond, C.; Saadaoui, H.; Furtado, C. A.; He, M.; Roubeau, O.; Ortolani, L.; Monthioux, M.; Pénicaud, A. Solutions of Negatively Charged Graphene Sheets and Ribbons. *J. Am. Chem. Soc.* **2008**, *130*, 15802−15804.

(39) Khan, U.; O'Neill, A.; Lotya, M.; De, S.; Coleman, J. N. High-Concentration Solvent Exfoliation of Graphene. *Small* **2010**, *6*, 864−871.

(40) Hasan, T.; Torrisi, F.; Sun, Z.; Popa, D.; Nicolosi, V.; Privitera, G.; Bonaccorso, F.; Ferrari, A. C. Solution-phase Exfoliation of Graphite for Ultrafast Photonics. *Phys. Status Solidi B* **2010**, *247*, 2953−2957.

(41) Hernandez, Y.; Lotya, M.; Rickard, D.; Bergin, S. D.; Coleman, J. N. Measurement of Multicomponent Solubility Parameters for Graphene Facilitates Solvent Discovery. *Langmuir* **2010**, *26*, 3208−3213.

(42) Bourlinos, A. B.; Georgakilas, V.; Zboril, R.; Steriotis, T. A.; Stubos, A. K. Liquid-Phase Exfoliation of Graphite Towards Solubilized Graphenes. *Small* **2009**, *5*, 1841−1845.

(43) Lotya, M.; Hernandez, Y.; King, P. J.; Smith, R. J.; Nicolosi, V.; Karlsson, L. S.; Blighe, F. M.; De, S.; Wang, Z.; McGovern, I. T.; Duesberg, G. S.; Coleman, J. N. Liquid Phase Production of Graphene by Exfoliation of Graphite in Surfactant/Water Solutions. *J. Am. Chem. Soc.* **2009**, *131*, 3611−3620.

(44) Bonaccorso, F.; Lombardo, A.; Hasan, T.; Sun, Z.; Colombo, L.; Ferrari, A. C. Production and Processing of Graphene and 2d Crystals. *Mater. Today* **2012**, *15*, 564−589.

(45) Torrisi, F.; Hasan, T.; Wu, W.; Sun, Z.; Lombardo, A.; Kulmala, T. S.; Hsieh, G.-W.; Jung, S.; Bonaccorso, F.; Paul, P. J.; Chu, D.; Ferrari, A. C. Inkjet-Printed Graphene Electronics. *ACS Nano* **2012**, *6*, 2992−3006.

(46) Santos, H. M.; Lodeiro, C.; Capelo-Martinez, J. L. The Power of Ultrasound. In *Ultrasound in Chemistry*; Capelo-Martinez, J. L., Ed.; Wiley-VCH Verlag GmbH & Co. KGaA: Weinheim, Germany, 2009; pp 1−15.

(47) Nascentes, C. C.; Korn, M.; Sousa, C. S.; Arruda, M. A. Z. Use of Ultrasonic Baths for Analytical Applications: A New Approach for Optimisation Conditions. *J. Braz. Chem. Soc.* **2001**, *12*, 57−63.

(48) Chivate, M. M.; Pandit, A. B. Quantification of Cavitation Intensity in Fluid Bulk. *Ultrason. Sonochem.* **1995**, *2*, S19−S25.

(49) McClements, D. J. Homogenization devices. In *Food Emulsions Principles, Practices, and Techniques*; CRC Press: Boca Raton, FL, 2005; pp 249−260.

(50) Secor, E. B.; Prabhumirashi, P. L.; Puntambekar, K.; Geier, M. l L.; Hersam, M. C. Inkjet Printing of High Conductivity, Flexible Graphene Patterns. *J. Phys. Chem. Lett.* **2013**, *4*, 1347−1351.

(51) Hyun, W. J.; Secor, E. B.; Hersam, M. C.; Frisbie, C. D.; Francis, L. F. High-Resolution Patterning of Graphene by Screen Printing with a Silicon Stencil for Highly Flexible Printed Electronics. *Adv. Mater.* **2015**, *27*, 109−115.

(52) Paton, K. R.; Varrla, E.; Backes, C.; Smith, R. J.; Khan, U.; O'Neill, A.; Boland, C.; Lotya, M.; Istrate, O. M.; King, P.; Higgins, T.; Barwich, S.; May, P.; Puczkarski, P.; Ahmed, I.; Moebius, M.; Pettersson, H.; Long, E.; Coelho, J.; O'Brien, S. E.; et al. Scalable Production of Large Quantities of Defect-free Few-Layer Graphene by Shear Exfoliation in Liquids. *Nat. Mater.* **2014**, *13*, 624−630.

(53) Barnes, H. A. What is Flow and Deformation?. In *A Handbook of Elementary Rheology*; Institute of Non-Newtonian Fluid Mechanics, University of Wales: Wales, U.K., 2004; pp 5−10.

(54) Atiemo-Obeng, V. A.; Calabrese, R. V. Rotor-Stator Mixing Devices. In *Handbook of Industrial Mixing: Science and Practice*; Paul, E. L., Atiemo-Obeng, V. A., Kresta, S. M., Eds.; John Wiley & Sons, Inc.: Hoboken, NJ, 2004; pp 479−505.

(55) Wang, J.; Manga, K. K.; Bao, Q.; Loh, K. P. High-Yield Synthesis of Few-Layer Graphene Flakes through Electrochemical Expansion of Graphite in Propylene Carbonate Electrolyte. *J. Am. Chem. Soc.* **2011**, *133*, 8888−8891.

(56) Panagiotou, T.; Mesite, S. V.; Bernard, J. M.; Chomistek, K. J.; Fisher, R. J. *Production of Polymer Nanosuspensions Using Microfluidizer Processor Based Technologies*; NSTI-Nanotech: Austin, TX, 2008; Vol. *1*, pp 688−691

(57) Goldberg, S. Mechanical/Physical Methods of Cell Disruption and Tissue. In *2D PAGE: Sample Preparation and Fractionation*; Posch, A., Ed; Humana Press: Totowa, NJ, 2008; pp 3−22.

(58) *Microfluidics International Corporation*. http://www.microfluidicscorp.com/ (accessed November 7, 2016).

(59) Lajunen, T.; Hisazumi, K.; Kanazawa, T.; Okada, H.; Seta, Y.; Yliperttula, M.; Urtti, A.; Takashima, Y. Topical Drug Delivery to Retinal Pigment Epithelium with Microfluidizer Produced Small Liposomes. *Eur. J. Pharm. Sci.* **2014**, *62*, 23−32.

(60) Tang, S. Y.; Shridharan, P.; Sivakumar, M. Impact of Process Parameters in the Generation of Novel Aspirin Nanoemulsions - Comparative Studies Between Ultrasound Cavitation and Micro-fluidizer. *Ultrason. Sonochem.* **2013**, *20*, 485−497.

(61) Jafari, S. M.; He, Y.; Bhandari, B. Production of Sub-micron Emulsions by Ultrasound and Microfluidization Techniques. *J. Food Eng.* **2007**, *82*, 478−488.

(62) Panagiotou, T.; Bernard, J. M.; Mesite, S. V. *Deagglomeration and Dispersion of Carbon Nanotubes Using Microfluidizer (R) High Shear Fluid Processors*; NSTI-Nanotech: Austin, TX, 2008; Vol. *1*, pp 39−42.

(63) dos Reis Benatto, G. A.; Roth, B.; Madsen, M. V.; Hösel, M.; Søndergaard, R. R.; Jørgensen, M.; Krebs, F. C. Carbon: The Ultimate Electrode Choice for Widely Distributed Polymer Solar Cells. *Adv. Energy Mater.* **2014**, *4*, 1400732.

(64) Gomes, H. L. Organic Field-Effect Transistors. In *Organic and Printed Electronics Fundamentals and Applications*; Nisato, G., Lupo, D., Ganz, S., Eds.; CRC Press: Boca Raton, FL, 2016; pp 147−197.

(65) *Imerys*. http://www.imerys-graphite-and-carbon.com/ (accessed November 7, 2016).

(66) Kouroupis-Agalou, K.; Liscio, A.; Treossi, E.; Ortolani, L.; Morandi, V.; Pugno, N. M.; Palermo, V. Fragmentation and Exfoliation of 2-dimensional Materials: A Statistical Approach. *Nanoscale* **2014**, *6*, 5926−5933.

(67) Moeck, P.; Rouvimov, S.; Rauch, E. F.; Véron, M.; Kirmse, H.; Häusler, I.; Neumann, W.; Bultreys, D.; Maniette, Y.; Nicolopoulos, S. High Spatial Resolution Semi-automatic Crystallite Orientation and Phase Mapping of Nanocrystals in Transmission Electron Micro-scopes. *Cryst. Res. Technol.* **2011**, *46*, 589−606.

(68) *Nanomegas*. http://nanomegas.com (accessed November 7, 2016).

(69) Gammer, C.; Burak-Ozdol, V.; Liebscher, C. H.; Minor, A. Diffraction Contrast Imaging Using Virtual Apertures. *Ultramicroscopy* **2015**, *155*, 1−10.

(70) Punckt, C.; Muckel, F.; Wolff, S.; Aksay, I. A.; Chavarin, C. A.; Bacher, G.; Mertin, W. The Effect of Degree of Reduction on the Electrical Properties of Functionalized Graphene Sheets. *Appl. Phys. Lett.* **2013**, *102*, 023114−023114−5.

(71) *ASTM E1131-08 Standard Test Method for Compositional Analysis by Thermogravimetry*; ASTM: West Conshohocken, PA, 2014.

(72) Shirley, D. A. High-Resolution X-Ray Photoemission Spectrum of the Valence Bands of Gold. *Phys. Rev. B* **1972**, *5*, 4709−4714.

(73) Welham, N. J.; Williams, J. S. Extended Milling of Graphite and Activated Carbon. *Carbon* **1998**, *36*, 1309−1315.

(74) Benson, J.; Xu, Q.; Wang, P.; Shen, Y.; Sun, L.; Wang, T.; Li, M.; Papakonstantinou, P. Tuning the Catalytic Activity of Graphene Nanosheets for Oxygen Reduction Reaction *via* Size and Thickness Reduction. *ACS Appl. Mater. Interfaces* **2014**, *6*, 19726−19736.

(75) *ASTM E1078-14 Standard Guide for Specimen Preparation and Mounting in Surface Analysis*; ASTM: West Conshohocken, PA, 2014.

(76) Moulder, J. F.; Stickle, W. F.; Sobol, P. E.; Bomben, K. D. *Handbook of X-ray Photoelectron Spectroscopy*; Perkin-Elmer: Eden Prairie, MN, 1992.

(77) Phaner-Goutorbe, M.; Sartre, A.; Porte, L. Soft Oxidation of Graphite Studied by XPS and STM. *Microsc., Microanal., Microstruct.* **1994**, *5*, 283−290.

(78) Briggs, D.; Seah, M. P. Practical Surface Analysis. *Auger and X-Ray Photoelectron Spectroscopy*; Wiley: Hoboken, NJ, 1990.

(79) Yang, D.; Velamakanni, A.; Bozoklu, G.; Park, S.; Stoller, M.; Piner, R. D.; Stankovich, S.; Jung, I.; Field, D. A.; Ventrice, C. A., Jr.; Ruoff, R. S. Chemical Analysis of Graphene Oxide Films after Heat and Chemical Treatments by X-ray Photoelectron and Micro-Raman Spectroscopy. *Carbon* **2009**, *47*, 145−152.

(80) Drewniak, S.; Muzyka, R.; Stolarczyk, A.; Pustelny, T.; Kotyczka-Morańska, M.; Setkiewicz, M. Studies of Reduced Graphene Oxide and Graphite Oxide in the Aspect of Their Possible Application in Gas Sensors. *Sensors* **2016**, *16*, 103.

(81) Haubner, K.; Murawski, J.; Olk, P.; Eng, L. M.; Ziegler, C.; Adolphi, B.; Jaehne, E. The Route to Functional Graphene Oxide. *ChemPhysChem* **2010**, *11*, 2131−2139.

(82) Tuinstra, F.; Koenig, J. L. Raman Spectrum of Graphite. *J. Chem. Phys.* **1970**, *53*, 1126−1130.

(83) Ferrari, A. C.; Robertson, J. Interpretation of Raman spectra of disordered and amorphous carbon. *Phys. Rev. B: Condens. Matter Mater. Phys.* **2000**, *61*, 14095−14107.

(84) Thomsen, C.; Reich, S. Double Resonant Raman Scattering in Graphite. *Phys. Rev. Lett.* **2000**, *85*, 5214−5217.

(85) Baranov, A. V.; Bekhterev, A. N.; Bobovich, Ya. S.; Petrov, V. I. Interpretation of Certain Characteristics in Raman Spectra of Graphite and Glassy Carbon. *Opt. Spectrosc.* **1987**, *62*, 612−616.

(86) Pocsik, I.; Hundhausen, M.; Koos, M.; Ley, L. Origin of the D Peak in the Raman Spectrum of Microcrystalline Graphite. *J. Non-Cryst. Solids* **1998**, *227-230*, 1083−1086.

(87) Piscanec, S.; Lazzeri, M.; Mauri, F.; Ferrari, A. C.; Robertson, J. Kohn Anomalies and Electron-Phonon Interactions in Graphite. *Phys. Rev. Lett.* **2004**, *93*, 185503.

(88) Ferrari, A. C.; Meyer, J. C.; Scardaci, V.; Casiraghi, C.; Lazzeri, M.; Mauri, F.; Piscanec, S.; Jiang, D.; Novoselov, K. S.; Roth, S.; Geim, A. K. Raman Spectrum of Graphene and Graphene Layers. *Phys. Rev. Lett.* **2006**, *97*, 187401.

(89) Basko, D. M.; Piscanec, S.; Ferrari, A. C. Electron-electron Interactions and Doping Dependence of the Two-Phonon Raman

Intensity in Graphene. *Phys. Rev. B: Condens. Matter Mater. Phys.* **2009**, *80*, 165413.

(90) Ferrari, A. C.; Basko, D. M. Raman Spectroscopy as a Versatile Tool for Studying the Properties of Graphene. *Nat. Nanotechnol.* **2013**, *8*, 235−246.

(91) Ferrari, A. C.; Robertson, J. Resonant Raman Spectroscopy of Disordered, Amorphous, and Diamondlike Carbon. *Phys. Rev. B: Condens. Matter Mater. Phys.* **2001**, *64*, 075414.

(92) Ferrari, A. C.; Rodil, S. E.; Robertson, J. Interpretation of Infrared and Raman Spectra of Amorphous Carbon Nitrides. *Phys. Rev. B: Condens. Matter Mater. Phys.* **2003**, *67*, 155306.

(93) Ferrari, A. C. Raman Spectroscopy of Graphene and Graphite: Disorder, Electron-Phonon Coupling, Doping and Nonadiabatic Effects. *Solid State Commun.* **2007**, *143*, 47−57.

(94) Parvez, K.; Wu, Z.-S.; Li, R.; Liu, X.; Graf, R.; Feng, X.; Müllen, K. Exfoliation of Graphite into Graphene in Aqueous Solutions of Inorganic Salts. *J. Am. Chem. Soc.* **2014**, *136*, 6083−6091.

(95) Pavlova, A. S.; Obraztsova, E. A.; Belkin, A. V.; Monat, C.; Rojo-Romeo, P.; Obraztsova, E. D. Liquid-Phase Exfoliation of Flaky Graphite. *J. Nanophotonics* **2016**, *10*, 012525.

(96) Ummartyotin, S.; Manuspiya, H. A Critical Review on Cellulose: From Fundamental to an Approach on Sensor Technology. *Renewable Sustainable Energy Rev.* **2015**, *41*, 402−412.

(97) Di Risio, S.; Yan, N. Piezoelectric Ink-Jet Printing of Horseradish Peroxidase: Effect of Ink Viscosity Modifiers on Activity. *Macromol. Rapid Commun.* **2007**, *28*, 1934−1940.

(98) Pavinatto, F. J.; Paschoal, C. W. A.; Arias, A. C. Printed and Flexible Biosensor for Antioxidants Using Interdigitated Ink-jetted Electrodes and Gravure-deposited Active Layer. *Biosens. Bioelectron.* **2015**, *67*, 553−559.

(99) Secco, R. A.; Kostic, M.; deBruyn, J. R. Fluid Viscosity Measurement. In *Measurement, Instrumentation, and Sensors Handbook Spatial, Mechanical, Thermal, and Radiation Measurement*; Webster, J. G., Eren, H.; CRC Press Taylor & Francis Group: Boca Raton, FL, 2014; pp 46−1.

(100) Mezger, T. G. *The Rheology Handbook: For Users of Rotational and Oscillatory Rheometers*; Vincentz Network GmbH & Co KG: Hannover, Germany, 2006.

(101) Lin, H.-W.; Chang, C.-P.; Hwu, W.-H.; Ger, M.-D. The Rheological Behaviors of Screen-Printing Pastes. *J. Mater. Process. Technol.* **2008**, *197*, 284−291.

(102) Benchabane, A.; Bekkour, K. Rheological properties of carboxymethyl cellulose (CMC) solutions. *Colloid Polym. Sci.* **2008**, *286*, 1173−1180.

(103) Nijenhuis, K.; McKinley, G. H.; Spiegelberg, S.; Barnes, H. A.; Aksel, N.; Heymann, L. A.; Odell, J. Thixotropy, Rheopexy, Yield Stress. In *Handbook Springer of Experimental Fluid Mechanics*, Tropea, C., Yarin, A. L., Foss, J. F., Eds.; Springer-Verlag: Berlin Heidelberg, 2007; pp 661−679.

(104) Irgens, F. *Rheology and Non-Newtonian Fluids*; Springer Verlag: Cham Heidelberg, 2014; pp 1−16.

(105) DeButts, E. H.; Hudy, J. A.; Elliott, J. H. Rheology of Sodium Carboxymethylcellulose Solutions. *Ind. Eng. Chem.* **1957**, *49*, 94−98.

(106) Elliot, J. H.; Ganz, A. J. Some Rheological Properties of Sodium Carboxymethylcellulose Solutions and Gels. *Rheol. Acta* **1974**, *13*, 670−674.

(107) Clasen, C.; Kulicke, W.-M. Determination of Viscoelastic and Rheo-optical Material Functions of Water-soluble Cellulose Derivatives. *Prog. Polym. Sci.* **2001**, *26*, 1839−1919.

(108) Steffe, J. F. *Rheological Methods in Food Process Engineering*; Freeman Press: East Lansing, MI 48823, USA, 1996.

(109) Roff, W. J.; Scott, J. R. *Fibres, Films, Plastics and Rubbers, A Handbook of Common Polymers*; Butterworths: London, 1971

(110) Xia, W.; Thorpe, M. F. Percolation Properties of Random Ellipses. *Phys. Rev. A: At., Mol., Opt. Phys.* **1988**, *38*, 2650−2656.

(111) Li, W.; Sun, B.; Wu, P. Study on Hydrogen Bonds of Carboxymethyl cellulose Sodium Film with Two-dimensional Correlation Infrared Spectroscopy. *Carbohydr. Polym.* **2009**, *78*, 454−461.

(112) Horvath, A. E.; Lindström, T. The Influence of Colloidal Interactions on Fiber Network Strength. *J. Colloid Interface Sci.* **2007**, *309*, 511−517.

(113) Dimiev, A. M.; Ceriotti, G.; Metzger, A.; Kim, N. D.; Tour, J. M. Chemical Mass Production of Graphene Nanoplatelets in ∼ 100% Yield. *ACS Nano* **2016**, *10*, 274−279.

(114) Arapov, K.; Rubingh, E.; Abbel, R.; Laven, J.; de With, G.; Friedrich, H. Conductive Screen Printing Inks by Gelation of Graphene Dispersions. *Adv. Funct. Mater.* **2016**, *26*, 586−593.

(115) Roy-Mayhew, J. D.; Bozym, D. J.; Punckt, C.; Aksay, I. A. Functionalized Graphene as a Catalytic Counter Electrode in Dye-Sensitized Solar Cells. *ACS Nano* **2010**, *4*, 6203−6211.

(116) Audioposter, http://www.audioposter.com/.

(117) Munson, B. R.; Young, D. F.; Okiishi, T. H.; Huebsch, W. W. *Fundamentals of Fluid Mechanics*; John Wiley & Sons, Inc.: Hoboken, NJ, 2009.

(118) Rouse, H. *Elementary Mechanics of Fluids*; Dover Publications Inc.: New York, 1946.

(119) Holman, J. P. *Heat Transfer*; McGraw-Hill: New York, 1986; pp 210.

(120) Siddiqui, S. W.; Zhao, Y.; Kukukova, A.; Kresta, S. M. Characteristics of a Confined Impinging Jet Reactor: Energy Dissipation, Homogeneous and Heterogeneous Reaction Products, and Effect of Unequal Flow. *Ind. Eng. Chem. Res.* **2009**, *48*, 7945−7958.

(121) Moody, L. F.; Princeton, N. J. Friction Factors for Pipe Flow. *Trans. ASME* **1944**, *66*, 671−684.

(122) Boxall, J. A.; Koh, C. A.; Sloan, E. D.; Sum, A. K.; Wu, D. T. Droplet Size Scaling of Water-in-Oil Emulsions under Turbulent Flow. *Langmuir* **2012**, *28*, 104−110.

(123) Zhang, J.; Xu, S.; Li, W. High Shear Mixers: A Review of Typical Applications and Studies on Power Draw, Flow Pattern, Energy Dissipation and Transfer Properties. *Chem. Eng. Process.* **2012**, *57-58*, 25−41.

(124) Kolmogorov, A. N. The Local Structure of Turbulence in Incompressible Viscous Fluids at very Large Reynolds Numbers. *Dokl. Akad. Nauk SSSR* **1941**, *30*, 299−303.

(125) Richardson, L. F. *Weather Prediction by Numerical Process*; Cambridge University Press: Cambridge, U.K., 1922; Vol. *48*, pp 282−284.

(126) Varrla, E.; Paton, K. R.; Backes, C.; Harvey, A.; Smith, R. J.; McCauley, J.; Coleman, J. N. Turbulence-assisted Shear Exfoliation of Graphene using Household Detergent and a Kitchen Blender. *Nanoscale* **2014**, *6*, 11810−11819.